Electronic Supplementary Material (ESI) for Journal of Materials Chemistry A.

Surface Reactions Between LiHMDS, TMA and TMP Leading to Deposition of Amorphous Lithium Phosphate: Supporting Information

Andreas Werbrouck[1], Felix Mattelaer[1], Arpan Dhara[1], Mikko Nisula[1], Matthias Minjauw[1], Frans Munnik[2], Jolien Dendooven[1], and Christophe Detavernier[1]

[1]Department of Solid State Sciences, Ghent University, Krijgslaan 281, Ghent, Belgium
[2]Ion Beam Center, Helmholtz-Zentrum Dresden-Rossendorf, Bautzner Landstraße 400, 01328 Dresden, Germany'

S1 Further process characterization

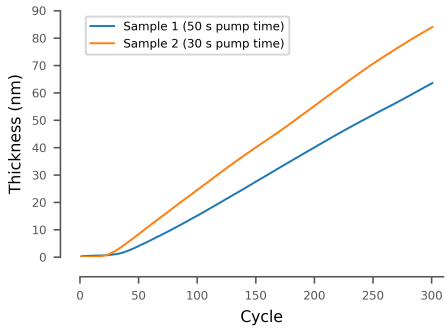

Figure S1: Thickness of the film as a function of number of cycles. A delay in growth can be observed, and while the growth is linear, it is dependent on the pump time.

LiHMDS		TMA		TMP		$OP(OCH_3)_2OAl(CH_3)(CH_2OCH_3)$		$OP(OCH_3)_2OAl(CH_3)(CH_2OCH_3)$ (cont.)	
m/z	ion	m/z	ion	m/z	ion	m/z	ion	m/z	ion
14	N	15	CH_3	15	CH_3	14	CH_2	95	OPOO
15	CH_3	27	Al	16	O	15	CH_3	103	$OAlCH_2OCH_3CH_3$
28	Si	42	$AlCH_3$	31	OCH_3	16	O	104	CH_2AlOPO
42	NSi	57	$Al(CH_3)_2$	47	PO	27	Al	105	$AlCH_3OPO_2$
43	$SiCH_3$	72	$Al(CH_3)_3$	62	$POCH_3$	30	OCH_2	106	OPOAlO
57	$NSiCH_3$			63	PO_2	31	OCH_3	109	$P(OCH_3)_2O$
58	$Si(CH_3)_2$			78	PO_2CH_3	41	$AlCH_2$	110	PO_4CH_3
70	NSi_2			79	PO_3	42	$AlCH_3$	119	CH_2AlCH_3OPO
72	$NSi(CH_3)_2$			93	$P(OCH_3)_2$	43	AlO	120	$AlCH_3OPOCH_3$
73	$Si(CH_3)_3$			94	PO_3CH_3	45	CH_2OCH_3	121	PO_3AlCH_3
85	NSi_2CH_3			95	PO_4	47	PO	122	PO_4Al
87	$NSi(CH_3)_3$			109	$PO_3(CH_3)_2$	56	$Al(CH_2)(CH_3)$	125	$OP(OCH_3)_2O$
100	$NSi_2(CH_3)_2$			110	PO_4CH_3	57	$AlOCH_2$	134	$POAlCH_2O(CH_3)_2$
115	$NSi_2(CH_3)_3$			124	$P(OCH_3)_3$	58	$Al(CH_3)O$	135	$AlOPOCH_2OCH_3$
130	$NSi_2(CH_3)_4$			125	$PO_4(CH_3)_2$	62	$POCH_3$	136	$AlOPO_2(CH_3)_2$
145	$NSi_2(CH_3)_5$			140	$PO_4(CH_3)_3$	63	OPO	137	PO_4AlCH_3
160	$NSi_2(CH_3)_6$					72	$Al(CH_3)O(CH_2)$	150	$PO_3AlCH_2(CH_3)_2$
						73	OCH_2AlO	151	$AlPO_3(CH_3)_3$
						74	AlOP	152	$AlPO_4(CH_3)_2$
						78	$POCH_3O$	165	$PO_3AlCH_2(CH_3)_3$
						79	OPOO	166	$PO_4AlCH_2(CH_3)_2$
						87	$AlCH_2OCH_3CH_3$	167	$AlPO_4(CH_3)_3$
						88	$AlOCH_2OCH_3$	181	$PO_4AlCH_2(CH_3)_3$
						89	$AlCH_3OP$	182	$OCH_2AlPO_4(CH_3)_2$
						90	AlOPO	196	$OCH_2AlPO_3(CH_3)_4$
						93	$P(OCH_3)_2$	197	$OCH_2AlPO_4(CH_3)_3$
						94	$OPOOCH_3$	212	$(CH_3)OCH_2Al(CH_3)PO_4(CH_3)_2$

Table S1: Theoretical mass over charge peaks for the relevant species. Note that sometimes multiple combinations of the mentioned atoms are possible, leading to the same mass. Where possible we have aimed for briefness in notation. Hydrogen capture can explain why sometimes the peak position is 1 unit higher than the indicated mass and is a known phenomenon in mass spectrometry[5]. To keep the fragmentation pattern clean, the CH_3 groups were treated as a single fragment for the calculation of possible fragments, so not every loss of a single hydrogen was considered. This may explain tails or peaks at lower m/z.

S2 QMS: peak identification

S2.1 Non negative Matrix Factorization

In order to separate the different contributions during the TMP pulse, a non-negative matrix factorization analysis (NMF[3, 1, 2]) was carried out on the observed time-resolved spectrum (fig. S3). This technique can be used to find the linearly independent, positive subcomponents of a number of high-dimensional vectors, even in the presence of noise. As such, it is ideally suited to decompose a QMS spectrum: if two species are present in the reactor at the same time, their fragments can both contribute to the signal at a shared mass (for example: a signal at m/z 15 may come from a TMP molecule (CH_3 fragment) or a (hypothetical) methane molecule (CH_3 fragment)). By comparing the signal of this mass with that of other masses at all times, it is possible to separate out the different contributions: the shape of the time-dependent signal at m/z 15 will be a scaled sum of the time-dependent signal from typical TMP peaks (e.g. m/z 140) and that from typical methane peaks (e.g. 12, 16). It is important to realize that no a priori assumptions on the nature of the species are made.

In this particular case, two components were identified: one constant and one transient. The constant component of the spectrum can clearly be identified as TMP (fig. S3b). The transient component contains some masses that would be part of the TMP spectrum, but as well a strong peak at 57, and, as mentioned before peaks at 197, 167, 137. We will start our interpretation at the m/z 137 fragment. It is tempting to assign the fragment to an ion consisting of a PO_4

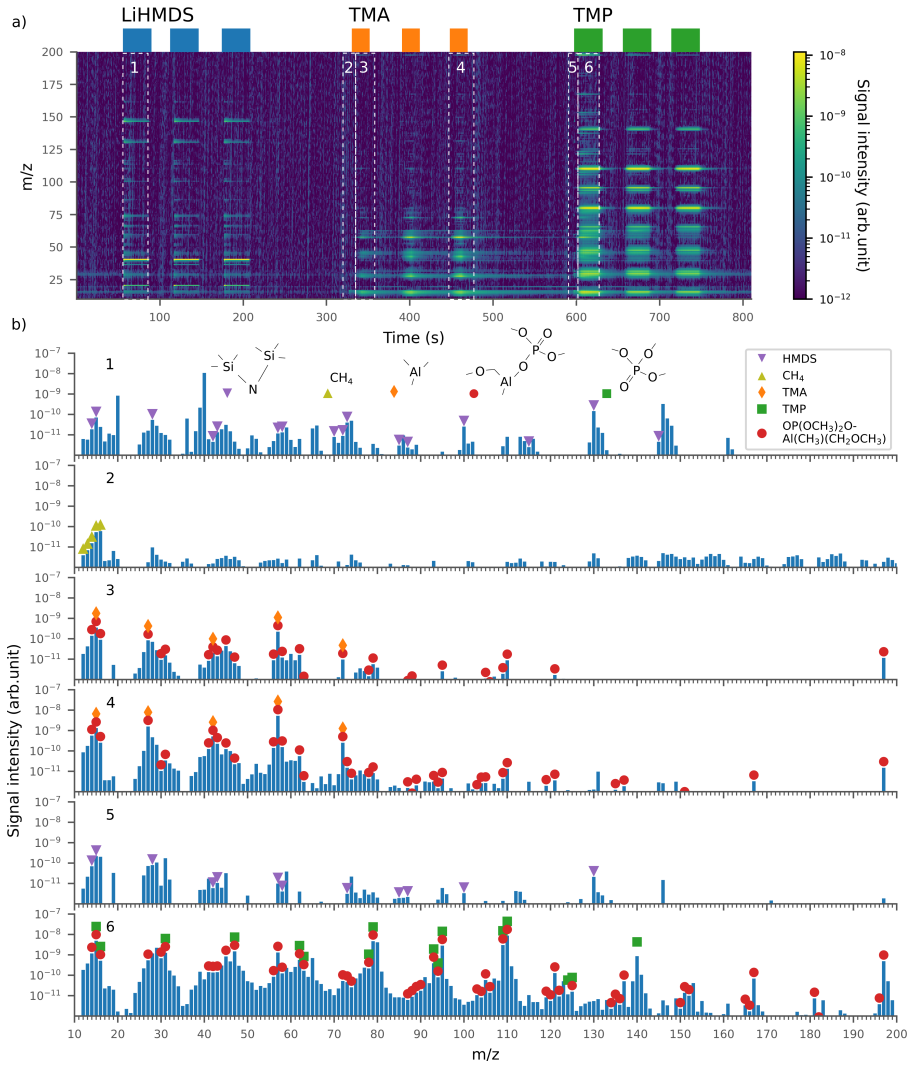

Figure S2: a) Mass spectrum of the TMA-enhanced process for a range m/z 0-200 where we characterized the process with about 1g 3μm diameter Al_2O_3 powder, at 325°C. b) Vertical slices of the data matrix shown above, integrated over the different zones as indicated. All theoretical fragments of the relevant species are indicated. Their height is dependent on the measured value. Deviations of m/z = 1 may occur due to proton capture, or by the fact that CH_3 units are considered indivisible. Inset: observed molecules.

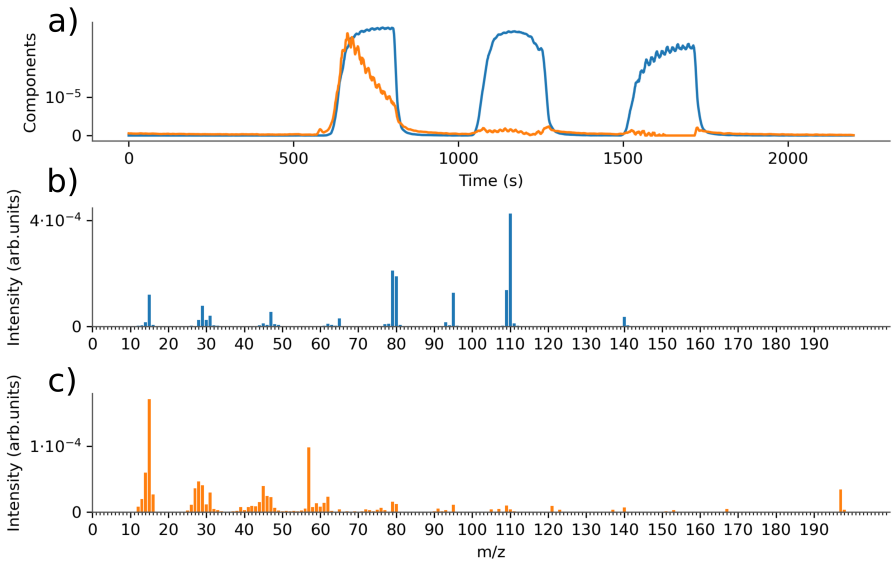

Figure S3: a) Non negative matrix factorization of the time-resolved spectrum during the TMP pulses resolves the observed spectrum (region 6 and later in fig. S2) into two components: b) a constant spectrum of TMP (blue) and c) a transient spectrum, turning out to be $OP(OCH_3)_2O\text{-}Al(CH_3)(CH_2OCH_3)$ (orange).

fragment combined with a $AlCH_3$ fragment. Adding a single methyl group (m/z 15) to this molecule brings us to 152, which is not in the spectrum, but 153 is. It might be that this fragment is more stable after capturing a hydrogen atom. One more methyl group brings us to m/z 167, which is prominently featured in the spectrum. We would like to add two more methyl groups to get to the highest peak of 197, but this is stoichiometrically impossible. Instead, we are reminded of the hydrogen abstraction reaction discussed previously, which led to an $AlCH_2O$ chain at the surface. The CH_2O fragment has also m/z 30, and moreover, minute, intermediate peaks at 181 (167 + 14 due to CH_2) and 183 can be observed as well. It is very likely that this chain is ended by another methyl group, leading to the molecule $OP(OCH_3)_2O - Al(CH_3)(CH_2OCH_3)$ (fragments and complete molecule indicated by the red dot in fig. S2b). This molecule has a mass of 212, meaning the upper limit of our measurement is slightly too low. Additional measurements did not confirm any signal at masses above 200, but it is possible that the ion of the full reaction product molecule is not stable enough to reach the detector.

S3 Electrochemical measurements

S3.1 Impedance spectroscopy

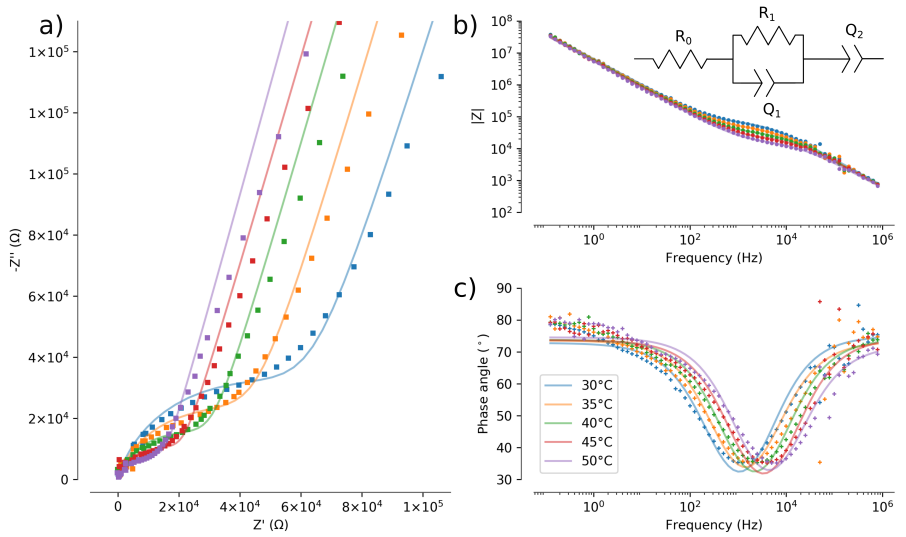

Figure S4: a) Nyquist plot of impedance data of a single dot with diameter 0.5 mm at different temperatures and the fit b) and c) Bode plot of the same data. Inset: equivalent circuit used to model the layer.

We attribute the first (series) resistance to the resistance of the cables and contacts, the first semicircle to the diffusion of the lithium ions in the film, and the constant phase element at the end (which is close to a capacitor) to the capacitive behavior of the MIM structure. An R(RQ)Q equivalent circuit can thus be used to fit the structure, where Q denotes a constant phase element and the brackets indicate a parallel circuit in Boukamp notation. Brief air exposure during unloading and to prepare the samples for sputtering might lead to a lithium carbonate layer, with a larger resistance [4]. In that case a R(RQ)(RQ)Q circuit should be used, where the second (RQ) element represents the conduction in the lithium carbonate.

The spectra were fitted both with R(RQ)Q and R(RQ)(RQ) equivalent circuits. The available data prohibits fitting the theoretical additional constant phase element in the latter case, which would dominate the spectrum at lower frequencies. All fits presented here use the R(RQ)Q circuit, which, despite its simplicity, yields good correspondence to the observed features. Using a R(RQ)(RQ) circuit, the resistance and conductivity values for the first semicircle were very similar, however for the R(RQ)(RQ) circuit fits, the uncertainty on the resistance for the second semicircle is very high, while the fit quality does not improve. Hence the simpler R(RQ)Q model is used.

Typically, a constant phase element Q is modeled using 2 parameters, an impedance Z (Ω) and a number between 0 and 1 determining the phase. If n=1, the element behaves like a capacitor. Physically meaningful fits were ensured

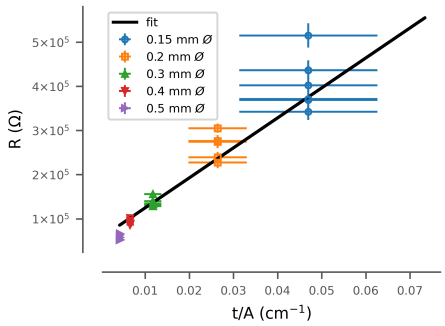

Figure S5: Results from fits to IS measurements at dots of different size, at 30°C (the lowest measurement temperature). The fitted resistance R_1 is plotted against $\frac{t}{A}$ with t the thickness of the film, and A the surface of the dot. Error bars in the y-direction are due to shadowing effects.

by constraining the parameters: for R_0 a lower bound was chosen at 10 Ω. R_1, Z_1, Z_2 were constrained to be positive and n_1 and n_2 were constrained between 0 and 1. R_0 is pushed towards 0 with an uncertainty of about 500Ω, as for the highest-frequency points the phase is already rather high (there is a nonzero imaginary contribution). As is expected, Z_1 varied along with R_1. Z_2 decreased with increasing diameter. The values for n_1 and n_2 were centered around 0.80, between 0.75 and 0.85.

As can be seen in figure S4, the fit is not perfect 'by the eye', especially not in the high frequency region, where the value of the phase does not seem to be constant. However, by the very nature of the fit algorithm, the fits shown reflect a minimum in the error function (fit-data)^2/modulus. The modulus weighing is common practice to allow working with the extremely large range of values in the data, and it explains why the low-frequency points are more off in the phase: the relative difference between the two is still very low. In the relevant parameter region (the small semicircle) the fit reproduces the behaviour of the data.

Often for these kind of analyses, only a couple of selected spectra are fitted in a very careful and constrained way. The fitted spectra only converge when parameters are allowed to vary in a narrow region. While there may be good reasons to assume more intricate equivalent circuits if one suspects different conduction mechanisms, such as R(RQ)(RQ) or R(RQ)(RQ)Q, this also inserts more parameters in the equation. The uncertainties on these parameters are very large here, hence it is not practical to use these circuits, especially not given the negligible influence of such a change in circuit on the first semicircle.

S3.2 DC polarization measurements

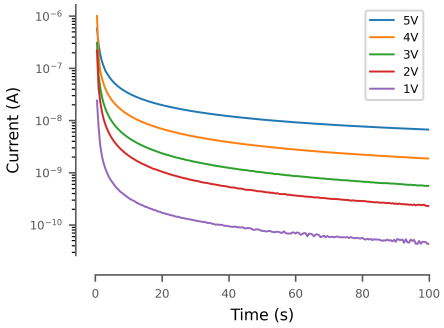

Figure S6: Electronic (DC) current measured on the same dot (diameter 0.4 mm), with different bias voltages. Note the non-linear relationship between the currents at different potentials.

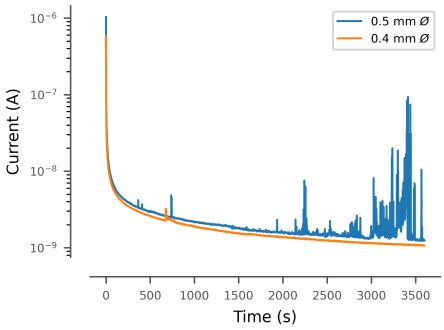

Figure S7: Electronic (DC) current measured on 2 dots, with bias voltage 5V. The dot with 0.4 mm diameter was the only one that made it to the end.

In order to determine through-plane electronic conductivity and cell stability, DC polarisation measurements were performed (figs. S6 and S7). For these measurements, we expect the following effects to dominate the measured current: initially, the ions in the film will move in order to compensate the charge buildup of electrons. As the ions cannot intercalate the Pt electrode, a double layer will form: the ions will gather at one side of the electrolyte film, in order to compensate for the build-up of electrons at the metal contact. After the formation of a double layer, effectively the entire potential difference is applied over this double layer. The only contribution to the current should be a very small, constant, leakage current of electrons. This current can then be used to determine the electronic conductivity of the film.

The same cell was measured for 100 s at the same potential, the potential was released for a while to allow the ions to settle back again, and then the cell was measured with a higher voltage. After ramping up the potential in this way to 5 V, we gauged the cell stability by measuring one more hour (fig. S7). Actually

even longer measurements are necessary to truly prove film stability: we see in fig. S6 that the final current does not settle to a constant value. It must be remarked that 5 V over a film with thickness of 84 nm results in an electric field strength of 60 MV/m, which is relatively high. What is striking under these conditions is that the current increases exponentially and not linearly with increasing potential, contrary to what is expected for measurements on the same, ohmic cell. Furthermore, the stability measurements were not straightforward. Cells broke down quite quickly after measurements started, and only a couple of cells made it to the 100 s at 5V. During the stability measurements only a single cell made it to the end of the 3600 s (fig. S7).

From these observations, we conclude that initially the film has good resistive properties for electrons. This can be inferred from the fact that we can actually see the exponential decrease of the ionic current. However, the film cannot withstand elevated potentials for a longer time. There are two possible mechanisms that may account for this: either the material readily starts to decompose or the double layer formed is not stable and the lithium is plated. Either of the two effects will give rise to an additional, exponentially decreasing current signal on top of the constant electronic leak current. After some time, the material breaks down, and the elevated currents from that point on further destroy the film. However, due to the promising ionic conductivity, further investigation into stabilising these films is warranted, and its application as an interfacial stabilising high-σ films is promising.

S3.3 Rate testing

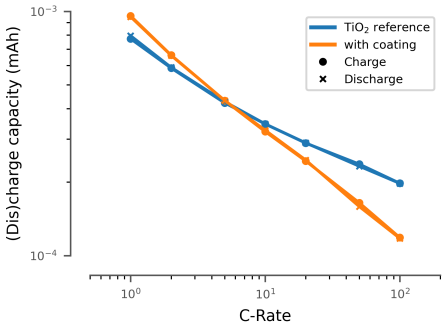

Figure S8: Capacity of a 40 nm thick, anatase TiO_2 cell with 0.96 cm^2 surface area as measured at various rates, coated and uncoated.

S3.4 Half-cell cycling

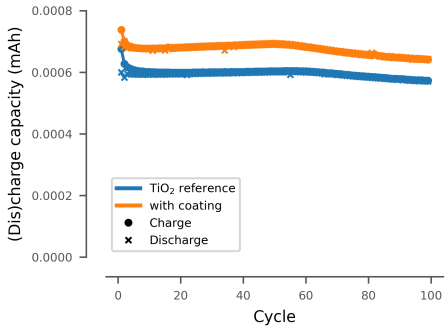

Figure S9: 2C Cycling capacity of a 40 nm thick, anatase TiO_2 cell with 0.96 cm^2 surface area, coated and uncoated.

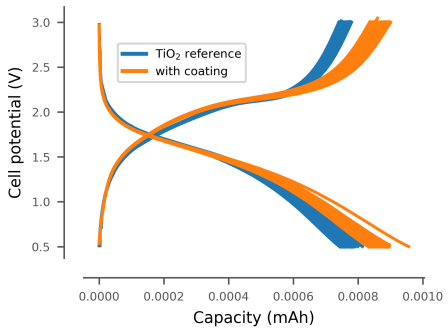

Figure S10: Voltage traces for the experiment in fig. S9

References

[1] A. Cichocki and A.-H. Phan. Fast local algorithms for large scale nonnegative matrix and tensor factorizations. *IEICE Transactions on Fundamentals of Electronics, Communications and Computer Sciences*, E92-A(3):708–721, 2009.

[2] C. Févotte and J. Idier. Algorithms for nonnegative matrix factorization with the β-divergence. *Neural Computation*, 23(9):2421–2456, 2011.

[3] D. D. Lee and H. S. Seung. Learning the parts of objects by non-negative matrix factorization. *Nature*, 401(6755):788–791, 1999-10.

[4] A. J. Pearse, T. E. Schmitt, E. J. Fuller, F. El-Gabaly, C.-F. Lin, K. Gerasopoulos, A. C. Kozen, A. A. Talin, G. Rubloff, and K. E. Gregorczyk. Nanoscale Solid State Batteries Enabled by Thermal Atomic Layer Deposition of a Lithium Polyphosphazene Solid State Electrolyte. *Chemistry of Materials*, 29(8):3740–3753, Apr. 2017.

[5] A. Werbrouck, M. Shirazi, F. Mattelaer, S. D. Elliott, J. Dendooven, and C. Detavernier. A Secondary Reaction Pathway for the Alumina Atomic Layer Deposition Process with Trimethylaluminum and Water, Revealed by Full-Range, Time-Resolved In Situ Mass Spectrometry. *The Journal of Physical Chemistry C*, pages 26443–26454, Nov. 2020. Publisher: American Chemical Society.